Extreme Mechanics Letters 42 (2021) 101065

Contents lists available at ScienceDirect

Extreme Mechanics Letters

journal homepage: www.elsevier.com/locate/eml

Bistability in popper-like shells programmed by geometric defects

Guangchao Wan [a,1], Yijie Cai [a,b,1], Yin Liu [a,c,1], Congran Jin [a], Dong Wang [d], Shicheng Huang [a], Nan Hu [e,*], John X.J. Zhang [a,*], Zi Chen [a,*]

[a] Thayer School of Engineering, Dartmouth College, Hanover, NH, 03755, USA
[b] School of Mechanical Engineering, Hubei University of Technology, Wuhan 430068, China
[c] School of Civil Engineering, Wuhan University, 8 South Road of East Lake, Wuchang, 430072 Wuhan, China
[d] Robotics Institute and State Key Laboratory of Mechanical System and Vibration, School of Mechanical Engineering, Shanghai Jiao Tong University, Shanghai, 200240, China
[e] School of Civil Engineering and Transportation, South China University of Technology, Guangzhou, 510641, China

ARTICLE INFO

Article history:
Received 21 August 2020
Received in revised form 16 October 2020
Accepted 18 October 2020
Available online 20 October 2020

Keywords:
Bistability
Spherical shells
Popper-like
Stability diagram
The Riks method

ABSTRACT

Bistable structures that can switch between two stable shapes are ubiquitous and have found applications in deployable structures, actuators, energy harvesters, etc. Among these, a bistable, spherical shell can stay stable in either the natural or "everted" shape. Previous works concentrate on the bistability of an intact shell, yet few efforts have been put into shells that feature a toy popper – a spherical shell with a circular hole located at its apex. To expand the existing design space of bistable shells, it is necessary to identify the quantitative relationship between the shell's bistability and the size of this geometric and topological defect. In this paper, through experiments, theory, and finite element analysis (FEA), we demonstrate that the bistability of a popper-like shell is mainly controlled by its geometric parameters and gets weakened initially and then enhanced as the relative size of the defect increases, indicating that a properly introduced defect can shift an intact shell from bistability to monostability or vice versa. Therefore, our research not only identifies the enriched design space of bistable shells, but also may advance the development of intelligent structures and devices such as smart switches and soft robotics, where the bistable shells can be employed.

1. Introduction

Bistable structures can adopt two stable shapes due to the interplay between geometry and mechanics [1,2]. The existence of two stable shapes and the accompanied shape transition (snap-through) can be utilized to fulfill specific purposes. For instance, the snap-through can be exploited to achieve fast morphological transitions [3–5] that have been exploited in nature and engineered system such as the fast closure of Venus flytrap (*Donaea muscipula*) [6], the ejection of the sporangium of *Polypodium aureum* [7] and robotics [8].

Among various bistable structures, spherical shells are commonly seen as components in engineered [9] and biological systems [10,11] across multiple length scales and thus have attracted great interest. A spherical shell can stay stable either as its original shape or as the "everted" shape when it is flipped. Regarding its bistability, previous research has demonstrated that it depends on the shell's geometry [12], material properties [13,14], inelastic deformation [15], boundary conditions [16], etc. To quantitatively seek the threshold that separates the bistability and monostability, researchers have adopted multiple theoretical frameworks such as the reduced Föppl–von Kármán (FvK) plate theory [17], shallow shell theory (Donnell–Mushtari–Vlasov model) [12], Koiter's deep shell theory [15] and finite element method (FEM) [18]. Furthermore, when integrated with stimuli-responsive materials, the bistable shell design has also facilitated fabricating shell-like actuators driven by magnetic field [19], responsive microlens in optical display [20] and colloidal particles that switch between two different morphologies [21].

For a shallow, spherical cap with linear elastic behavior, the bistability heavily depends on its geometry. For example, researchers have identified a dimensionless parameter $\lambda = R\alpha^2/h$ that controls the bistability of the shell [12,13], where R is the radius of the shell, α is the half of the shell's subtended angle and h is the shell's thickness. Only when λ is larger than the threshold λ_c can the shell become bistable (λ_c is related to the Poisson's ratio ν of the constituent material). Such a criterion provides much information for controlling the shell's bistability yet indicates certain limitation of the bistable shell's performance. For instance, when its subtended angle and radius are fixed, there exists a critical thickness beyond which the shell loses bistability. This

* Corresponding authors.
E-mail addresses: nanhu026@scut.edu.cn (N. Hu), John.Zhang@dartmouth.edu (J.X.J. Zhang), zi.chen@dartmouth.edu (Z. Chen).
[1] Equal contribution.

https://doi.org/10.1016/j.eml.2020.101065
2352-4316/

limitation on the thickness may restrict the energy output when the bistable shell is utilized as an actuator or energy harvester, since the shell's bending energy U_b and stretching energy U_s scale as $U_b \sim Eh^3$, $U_s \sim Eh$ (E is the Young's modulus). Therefore, to increase the adaptability of bistable shells in applications, it is of interest to introduce additional variables to enrich the current design space.

Here, inspired by the toy popper (Fig. 1(a)), we introduce a circular hole at the shell's apex and intend to examine the relationship between the size of this well-defined, topological defect and the bistability of the shell. A better understanding of this quantitative relationship will broaden the applications of bistable shells for two reasons. First, such a geometric defect can be introduced unintentionally during manufacturing, so it is necessary to identify its influence on the shell's bistability. Second, geometric defects such as holes and cuts can be employed in order to achieve extraordinary properties. Examples include the encapsulation of a "Buckliball" under pressure [22], the bistable Miura-ori origami unit with pop-through defect [23] and the ancient kirigami technique in which the deliberately introduced cuts enable the paper to undergo various intricate deformations that are not accessible for the intact paper [24–26]. Therefore, the results from this quantitative study will allow us to tune the mechanical performances of a bistable shell if we can intentionally introduce geometric voids. Specifically, we intend to answer the following questions regarding the bistability of such a popper-like shell: how does the hole affect the deflection and stress distribution of the "everted" shell? What is the bifurcation type? How to quantitatively construct the stability diagram in terms of the hole's size that can guide the future design of this bistable, defected shell? What advantages does a popper-like shell have as compared to an intact shell? Sobota, et al. [27] theoretically investigated this problem for the shallow shell case in the absence of experiments. In this study, we aim to address the above questions for the deep shell case by a combination of experiments, theoretical analysis and FEA.

The rest of the paper is organized as follows. In Section 2, we introduce the experiment setup that is utilized to test the popper-like shell's bistability. The theoretical analysis is presented in Section 3. Section 4 illustrates the procedures in the commercial software ABAQUS to study the bistable behavior of a popper-like shell. The main results are provided and discussed in Section 5. Section 6 presents conclusions and future directions.

2. Experiments

The geometry of the popper-like shell is schematically shown in Fig. 1(b). The thickness of the shell is h. The radius and half of the subtended angle of the shell's middle surface are R and α, respectively. A circular hole is located at the shell's apex with half of its subtended angle α_0. In experiments, we fabricated the shells by pouring the uncured silicon rubber into the 3D-printed mold. Once the solidification is finished, the shells can be peeled off from the mold. The specimen has the Young's modulus of 0.8 MPa and the Poisson's ratio of 0.44.

To quantitatively determine the shell's bistability, we perform the indention test by using the INSTRON universal test machine that can output the force–displacement relationship during the indention process (Fig. 2(a)–(b)). The indenter moves downwards with a constant speed 100 mm/min. At the same time, the shell is placed on a metal plate with a circular hole at its center that accommodates the shell's deformation. If a shell is bistable, it will snap to its everted shape once the indenter's displacement is beyond a critical value (Fig. 2(c)). Otherwise it will retreat to its original shape following the indenter, indicating monostability (Fig. 2(d)). Although in experiments the force–displacement relationship may depend on many factors including the relative size of the indenter, in this study we limit our discussion to the shell's bistability that is only governed by the shell's geometry and material property. More experimental cases and videos can be found in Supplementary Information.

3. Theory

To rationalize the bistable behavior of a popper-like shell theoretically, we resort to the Donnell–Mushtari–Vlasov (DMV) theory that describes the mechanics of a shallow shell with large deflection [28]. Although the DMV equations are derived based on the shallow shell assumption ($\alpha \ll 1$), the previous research has demonstrated that such a model can work well for the bistability of a deep, intact shell with the subtended angle α reaching up to $\sim$1.2 [12]. We express the governing equations in the cylindrical coordinate (r, θ, z), where the shell's apex is located at the z axis while the shell's planform spans the (r, θ) plane (Fig. 1(b)). Owing to the axisymmetric deflection of the shell, all the differentiations with respect to the azimuthal angle θ disappear, and the governing equations follow [12]

$$\begin{aligned} &\frac{1}{E}\nabla^4\phi + \frac{1}{r}\frac{dw}{dr}\frac{d^2w}{dr^2} - \frac{1}{R}\nabla^2 w = 0 \\ &D\nabla^4 w - \frac{h}{r}\frac{d}{dr}\left(\frac{dw}{dr}\frac{d\phi}{dr}\right) + \frac{h}{R}\nabla^2\phi = 0 \end{aligned} \tag{1}$$

where E is the Young's modulus, $\nabla^2 = d^2/dr^2 + d/rdr$ is the Laplacian operator, ϕ is the Airy stress function and the in-plane stress components σ_{rr} and $\sigma_{\theta\theta}$ are given as $\sigma_{rr} = d\phi/rdr$ and $\sigma_{\theta\theta} = d^2\phi/dr^2$ ($\sigma_{r\theta} = 0$ because $d/d\theta = 0$), w is the transverse displacement of the shell along the z direction, $D = Eh^3/12\left(1-\nu^2\right)$ is the bending rigidity. The first equation in Eq. (1) describes the geometric compatibility of the in-plane strain components, whereas the second equation depicts the force balance normal to the middle surface of the shell. The in-plane force balance is automatically satisfied by the introduction of the Airy stress function.

Eq. (1) contains two coupled, fourth-ordered differential equations where the analytical solution seems impossible. However, based on certain assumption, one can reduce the system's degrees of freedom and obtain closed-form results that can offer qualitative insight into the shell's bistability. Here, we adopt the assumption that the deformed shell has a uniform distribution of curvature $\kappa = -d^2z/dr^2 = const$ [29]. Accordingly, the stretching energy U_s and bending energy U_b can be expressed with one degree of freedom κ as $U_s = \pi Eh/384\left(b^2-a^2\right)^3\left(\kappa^2-{\kappa_0}^2\right)^2$ and $U_b = \pi Eh^3\left(b^2-a^2\right)(\kappa-\kappa_0)^2/12\,(1-\nu)$ ($\kappa_0 = 1/R$, SI). Through seeking the local minima of the total elastic energy by the conditions $\partial\left(U_s+U_b\right)/\partial\kappa = 0$, $\partial^2\left(U_s+U_b\right)/\partial\kappa^2 > 0$, we obtain an equation as $(\tilde{\kappa}-1)\left[1+(1-\nu)R^2\left(\alpha^2-{\alpha_0}^2\right)^2\tilde{\kappa}\left(\tilde{\kappa}+1\right)/16h^2\right] = 0$, where $\tilde{\kappa} = R\kappa$ is the dimensionless curvature. This equation is satisfied by letting either $\tilde{\kappa} = 1$ or $\tilde{\kappa}\left(\tilde{\kappa}+1\right) + 16h^2/(1-\nu)R^2\left(\alpha^2-{\alpha_0}^2\right)^2 = 0$. The first equation denotes the stress-free, natural shape while one of the real roots of the latter quadratic equation represents the stable, "everted" shape. By solving the quadratic equation, we can introduce a dimensionless parameter $\eta = \left(\alpha^2-{\alpha_0}^2\right)/(h/R)$. Only when η is greater than a threshold $\eta_c = 8/\sqrt{1-\nu}$ can the shell become bistable. Judging from η, we can tell that the introduced hole weakens the shell's bistability because η decreases as the hole's size α_0 increases while the threshold η_c is unchanged. By plotting all the equilibrium solutions together, we can obtain the bifurcation diagram with respect to the reduced curvature $\tilde{\kappa}$ and the control parameter η. As shown in Fig. 3(a), the stable "everted" shape annihilates

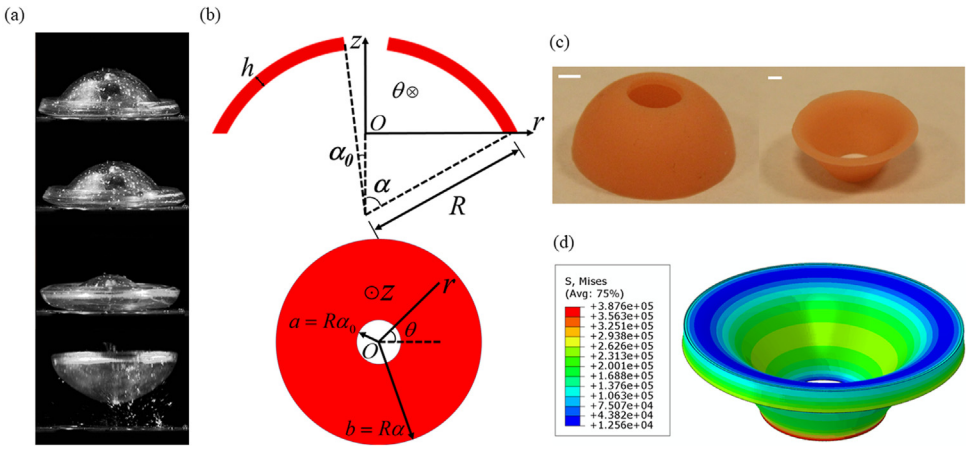

Fig. 1. (a) Snap-through of a toy popper. (b) Schematic illustration of the geometry of the popper-like shell. (c) The natural (left) and "everted" (right) shape of a popper-like shell. The geometric parameters are $R = 10$ mm, $h = 2$ mm, $\alpha = 90°$, $\alpha_0 = 23.6°$. The scale bars are 3 mm. (d) The FEA result of the distribution of Von Mises stress (Pa) within the "everted" shell.

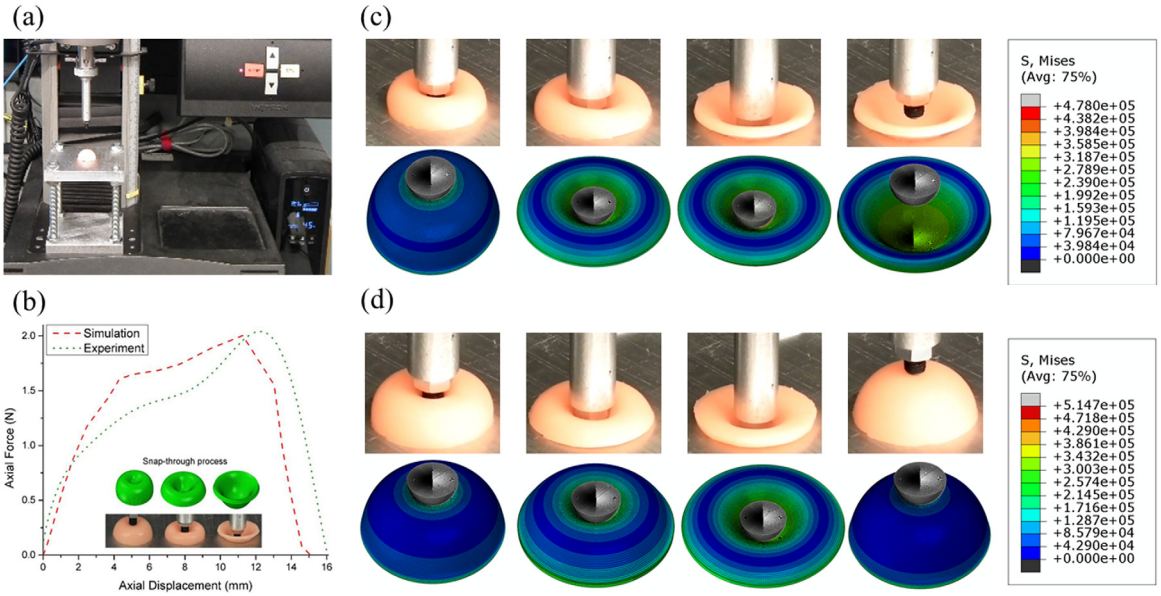

Fig. 2. (a) The INSTRON universal test machine. (b) The force–displacement relationships that are output from experiments and FEA. (c) The indention test of a bistable shell in experiments (first row) and FEA (second row). The shell's geometry is determined by the following parameters, $\alpha = 90°$, $\alpha_0 = 0°$, $R = 10$ mm, $h = 2.2$ mm. (d) The indention test of a monostable shell in experiments (first row) and FEA (second row). The shell's geometry is determined by the following parameters, $\alpha = 90°$, $\alpha_0 = 0°$, $R = 10$ mm, $h = 2.5$ mm. The unit of Von Mises stress is Pa.

the unstable yet equilibrium shape when η reaches the threshold $\eta_c \approx 10.69$, indicating that the popper-like shell undergoes a saddle–node bifurcation when its bistability is lost.

The assumption of uniform curvature distribution violates the boundary conditions at the free edges where the bending moment and shear force should be zero. It causes errors with respect to the shell's displacement and stress distribution. For instance, the uniform curvature assumption suggests that the outline of the everted shell's middle surface in the r-z plane should be convex ($d^2z/dr^2>0$), in contrast to the experimental observation where the outline is concave ($d^2z/dr^2 < 0$). Therefore, we need alternative methods to capture the shape of the "everted" shell and the bifurcation threshold more accurately. One feasible way is to increase the degrees of freedom without significantly increasing the computation by assuming some specific ansatz of the displacement $w(r)$ as a polynomial expression proposed by Sobota et al. [16], and this theoretical procedure is adopted in this study for further comparison (SI).

In addition to choosing a presumption of the shell's deflection, we can numerically solve the governing equations Eq. (1). For convenience, we non-dimensionalize Eq. (1) by introducing the reduced parameters as $\tilde{w} = wR/\left(b^2 - a^2\right)$, $\tilde{r} = r/\sqrt{b^2 - a^2}$, $\tilde{\phi} = \phi R^2/E\left(b^2 - a^2\right)^2$, and the dimensionless governing equations take the form as

$$\tilde{\nabla}^4\tilde{\phi} + \frac{1}{\tilde{r}}\frac{d\tilde{w}}{d\tilde{r}}\frac{d^2\tilde{w}}{d\tilde{r}^2} - \tilde{\nabla}^2\tilde{w} = 0$$
$$\frac{1}{12\left(1-\nu^2\right)\eta^2}\tilde{\nabla}^4\tilde{w} - \frac{1}{\tilde{r}}\frac{d}{d\tilde{r}}\left(\frac{d\tilde{w}}{d\tilde{r}}\frac{d\tilde{\phi}}{d\tilde{r}}\right) + \tilde{\nabla}^2\phi = 0 \quad (2)$$

Following the experimental setup, we choose the simply supported boundary conditions, i.e., the bending moment, shear force and in-plane radial stress are zero at the shell's edges. In addition, the outer edge of the shell is fixed along the z direction to avoid rigid body motion. Specifically, the eight boundary conditions that complete this boundary value problem are given in Table 1, where $\tilde{\nabla} = d^2/d\tilde{r}^2 + d/\tilde{r}d\tilde{r}$ is the Laplacian operator with respect

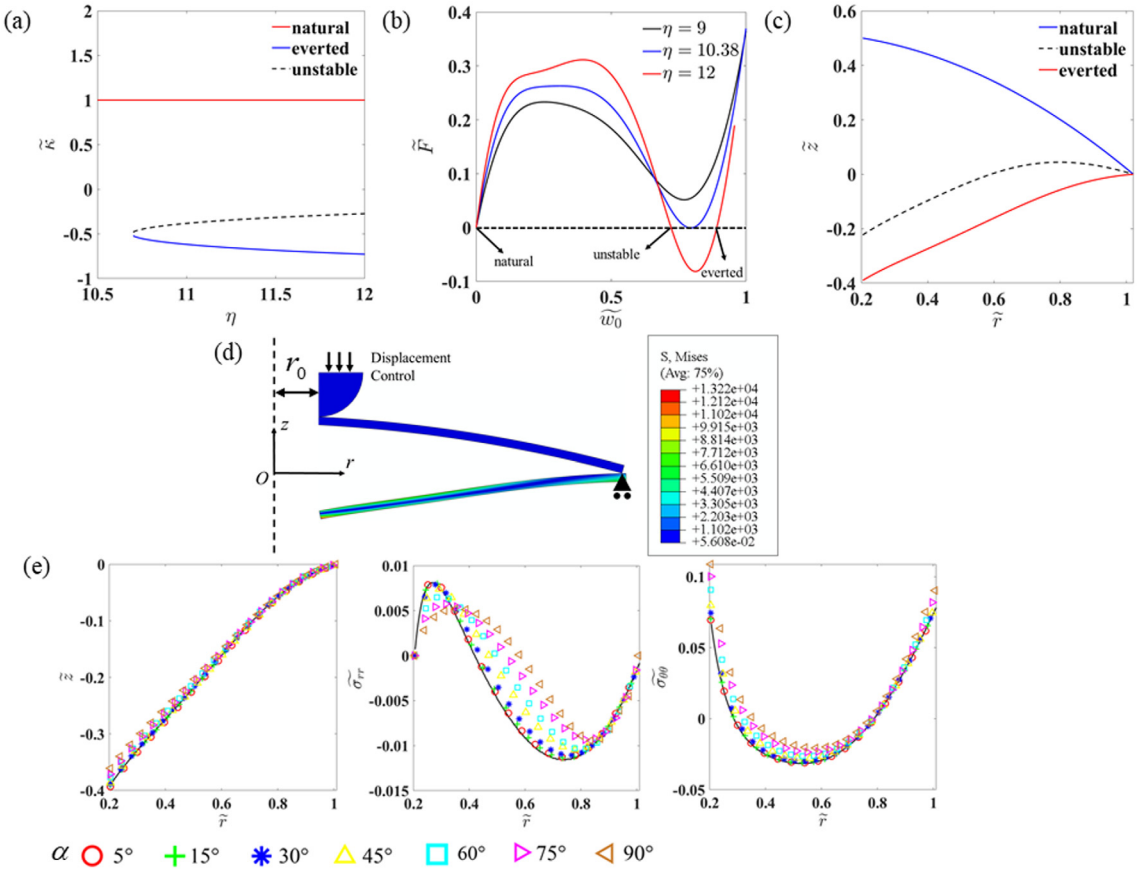

Fig. 3. (a) Bifurcation diagram based on the uniform curvature assumption. (b) Force–displacement relationships calculated from the Riks method. (c) The configurations of the natural shape (red solid), the unstable yet equilibrium shape (black dashed) and the stable "everted" shape (blue solid) from the Riks method. (d) The geometry model in ABAQUS. The dashed line is the axisymmetric axis. The unit of Von Mises stress is Pa. (e) The distribution of $\tilde{z}$, $\widetilde{\sigma_{rr}}$ and $\widetilde{\sigma_{\theta\theta}}$ versus $\tilde{r}$ in the "everted" shape. For all cases, $\eta = 12$, $\beta = 0.2$, $\nu = 0.44$. The black solid line is predicted from the Riks method and the dots are from FEA with different values of α. . (For interpretation of the references to color in this figure legend, the reader is referred to the web version of this article.)

Table 1
The eight boundary conditions that complete the boundary value problems. $\widetilde{M_r}$, $\widetilde{q_r}$ and $\widetilde{\sigma_{rr}}$ represent the dimensionless bending moment, shear force and in-plane radial stress component, respectively.

Zero bending moment, shear force and in-plane radial stress at $\tilde{r} = \widetilde{r_0} = \beta/\sqrt{1-\beta^2}$ and $\tilde{r} = \widetilde{r_1} = 1/\sqrt{1-\beta^2}$	$\widetilde{M_r} \sim d^2\tilde{w}/d\tilde{r}^2 + (\nu/\tilde{r})\, d\tilde{w}/d\tilde{r} = 0$
	$\widetilde{q_r} \sim d^3\tilde{w}/d\tilde{r}^3 + (1/\tilde{r})\, d^2\tilde{w}/d\tilde{r}^2 - (1/\tilde{r})^2\, d\tilde{w}/d\tilde{r} = 0$
	$\widetilde{\sigma_{rr}} \sim d\tilde{\phi}/d\tilde{r} = 0$
Fixed z-directional displacement $\tilde{r} = \widetilde{r_1} = 1/\sqrt{1-\beta^2}$	$\tilde{w} = 0$ $\tilde{\phi} = 0$

to the reduced radial coordinate. From the dimensionless governing equations and the corresponding boundary conditions, we can identify three control parameters that determine the system's bistability, i.e., η, $\beta = \alpha_0/\alpha$ and the Poisson's ratio ν. The first two parameters are purely geometric. η measures the ratio of the shell's stretching energy and bending energy [12] while β measures the relative size of the geometrical defect. In the meantime, the emergence of the Poisson's ratio in Eq. (2) indicates that the shell's bistability is also affected by the material property. Apart from these three parameters, the shell's depth, which can be represented as the half of the subtended angle α, should also affect the shell's bistability. However, this dimensionless parameter does not appear in a shallow shell theory.

To numerically solve the DMV equations, we resort to the Riks method that can output the non-monotonic evolution of the equilibrium path and thus capture both stable and unstable shapes of the shell with given boundary conditions [30,31]. Specifically, in the simulation, we apply a point load F at the inner edge of the shell to push the shell downwards. Both the magnitude of the point load and the shell's displacement are introduced as unknowns and solved by combining the discretized governing equations and an arc-length method, enabling to automatically trace the equilibrium paths in both stable and unstable regimes (SI). If the defected shell is bistable, the snap-through should happen when the point load increases to a critical value, and the structure can maintain another stable shape after the applied load is withdrawn. Several force–displacement relationships with different values of η are shown in Fig. 3(b). In all these cases, $\nu = 0.44$, $\beta = 0.2$, the magnitude of the force F is non-dimensionalized as $\tilde{F} = FR/Eh^3$ and the transverse displacement of the shell's inner edge w_0 is reduced as $\widetilde{w_0} = w_0 R/(b^2 - a^2)$. When $\eta = 12$, the force–displacement curve crosses the line $\tilde{F} = 0$ at three locations, corresponding to the natural shape, unstable yet equilibrium shape and the stable "everted" shape, respectively (Fig. 3(c)). When η decreases to 10.38, the curve tangentially intersects the line $\tilde{F} = 0$, suggesting the transition from bistability to monostability. As η further decreases ($\eta = 9$),

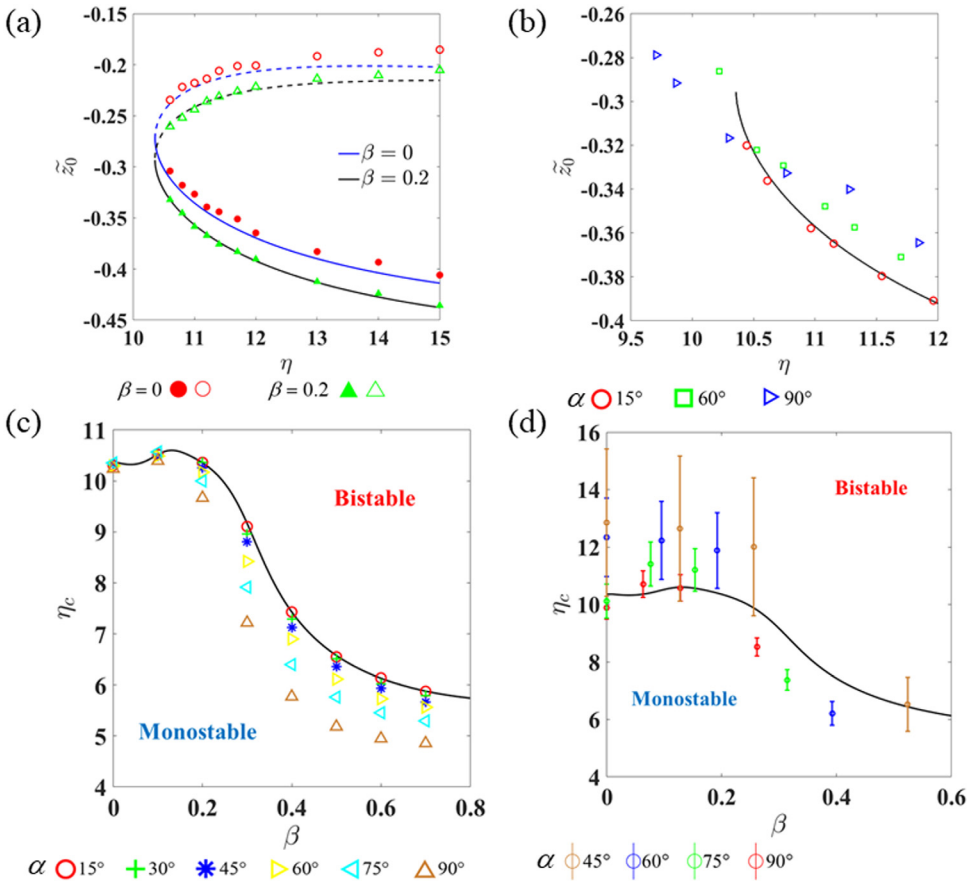

Fig. 4. (a) Bifurcation diagrams with respect to $\widetilde{z}_0$ and η ($\nu = 0.44$). The curves are calculated based on the polynomial ansatz and the data points are from the Riks method. The solid curves (filled points) represent the stable "everted" shape while the dashed curves (unfilled points) represent the unstable yet equilibrium shape. (b) Comparison of the theoretical results (curve) and FEA (data points) regarding the bifurcation diagram. $\eta = 12$, $\beta = 0.2$, $\nu = 0.44$. (c) Stability diagram with respect to η_c and β ($\nu = 0.44$). The solid curve is the threshold from the theoretical analysis (polynomial ansatz) while the unfilled dots are the thresholds from FEA with accuracy ± 0.1. (d) Comparison of the theory (polynomial ansatz) and experiments regarding the stability diagram.

the force–displacement curve only crosses the line $\tilde{F} = 0$ when $\widetilde{w_0} = 0$, indicating that the only shape in equilibrium without the external force is the natural shape and the bistability is thus lost.

4. Finite element analysis (FEA)

To verify the experimental results and testify the ability of the shallow shell theory in the deep shell situation, we performed FEA on the popper-like shell in ABAQUS. Previous studies have demonstrated the capability of FEA to predict the shapes [29,32], bifurcation thresholds [33] and snap-through processes [34] of bistable structures. Besides, FEA allows us to explore the popper-like shell's bistability with lower cost than experiments in a wider parametric regime.

Owing to the axisymmetric characteristic of the shell's deflection, we simplify the problem as a two-dimensional (2D) model (Fig. 3(d)). The simulation is conducted in two steps. In the first step, dynamic implicit analysis is performed in which the rigid indenter moves downwards and pushes the shell to its "everted" shape. The indenter then goes back to its initial position in the second step to let the shell seek its equilibrium shape around the "everted" state under the general static analysis. To reproduce the experimental setup, the vertical translation along the z axis is restrained at inner bottom edge (Fig. 3(d)). Other detailed information can be found in Supplementary Information. As shown in Fig. 2(c)–(d), the experimental indention test on a bistable or monostable shell can be well captured by FEA and qualitative agreement is found between the experiments and simulation regarding the load–displacement curve (Fig. 2(b)). The discrepancy, we assume, results from the friction between the shell and the indenter and between the shell and the metal plate in experiments that we cannot quantitatively reproduce in FEA.

5. Results and discussions

First, we compare the theoretical results with FEA regarding the deflection ($\tilde{z} = zR/\left(b^2 - a^2\right)$) and stress distribution ($\widetilde{\sigma_{rr}} = \sigma_{rr}/E\left(\alpha^2 - {\alpha_0}^2\right)$, $\widetilde{\sigma_{\theta\theta}} = \sigma_{\theta\theta}/E\left(\alpha^2 - {\alpha_0}^2\right)$) of the "everted" shape. In FEA, these variables are output from the middle surface of the shell. As shown in Fig. 3(e), the data points from FEA cluster when the shell is shallow. For the configuration $\tilde{z}$, the cluster holds when α reaches 60° while for the in-plane stress $\widetilde{\sigma_{rr}}$ and $\widetilde{\sigma_{\theta\theta}}$, such a cluster only holds when α reaches 30°. The clustered points fall around the master curve predicted from the theory, suggesting the good agreement between the theory and FEA when the shell is shallow. Besides, the data clustering indicates that the shallow shell theory has reasonable accuracy in predicting the popper-like shell's deflection and stress distribution when $\alpha < 30°$ (for the deflection alone, the limit can be extended to 60°). Nevertheless, when the shell gets deeper such as $\alpha = 75°$ or 90°, significant discrepancy appears between the theory and FEA, implying the limitation of the shallow shell assumption.

Based on the verified DMV model, we plot the bifurcation diagram of the popper-like shell by putting all branches of equilibrium solutions together. As shown in Fig. 4(a), we plot the

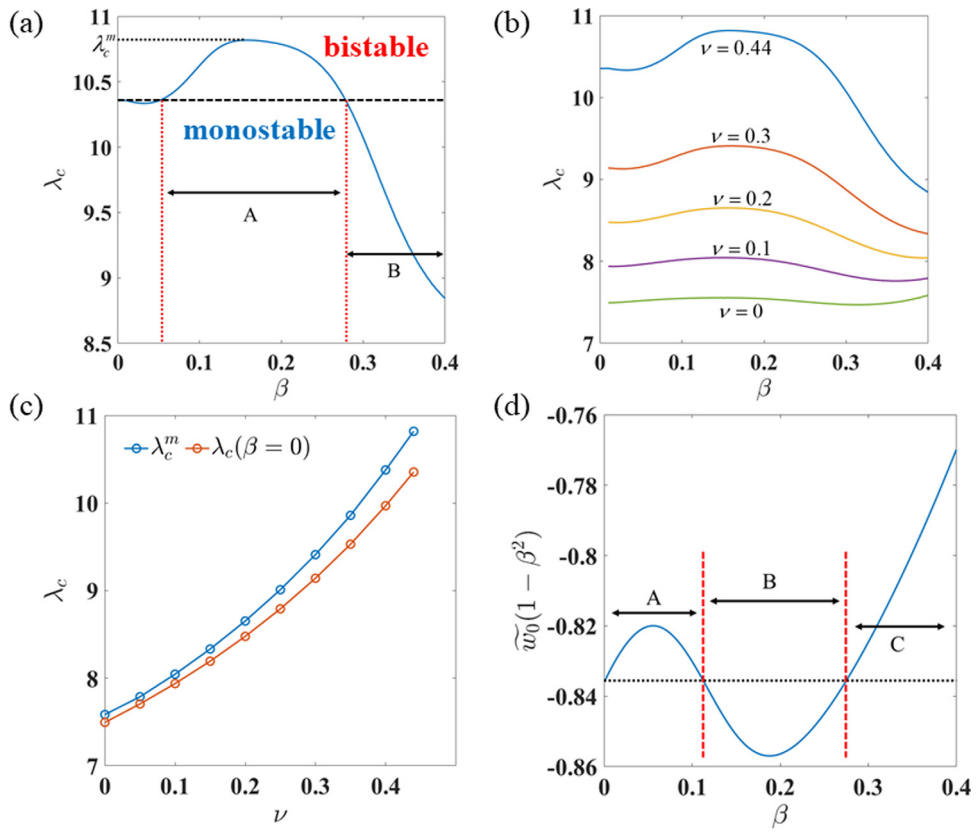

Fig. 5. (a) Stability diagrams with respect to λ_c and β. The intact shell's bistability is weakened in the regime A and enhanced in the regime B. (b) Stability diagrams with respect to λ_c and β when ν chooses different values. (c) Variations of λ_c^m and λ_c of an intact shell versus ν. (d) Variation of the maximum deflection of the popper-like shell $\widetilde{w_0}\left(1-\beta^2\right)$ versus β.

bifurcation diagram of an intact shell ($\beta = 0$) and a popper-like shell ($\beta = 0.2$) with respect to the reduced coordinate of the shell's inner edge $\widetilde{z_0} = \tilde{z}\left(\tilde{r} = \widetilde{r_0}\right)$ when η varies. The stable "everted" solution will annihilate another unstable equilibrium shape when η reaches the threshold η_c. It shows that the system undergoes the saddle–node bifurcation, which agrees with the analysis based on the uniform curvature assumption. We also compare the bifurcation diagram from the DMV theory with FEA. For instance, when $\beta = 0.2$, in the shallow shell case ($\alpha = 15°$), the data points from FEA are close to the theoretical prediction (Fig. 4(b)). While in the deep shell cases ($\alpha = 60°, 90°$), the inaccuracy of the theoretical results gets significant.

The bifurcation diagrams show that the relative size of the defect (β) has a significant impact on the shell's bistability (η_c). Accordingly, by capturing η_c as β changes, we can construct the stability diagram that quantitatively measures the effect of the hole's size on the shell's bistability (Fig. 4(c)). The threshold η_c undergoes a non-monotonic change as β increases — when β increases from 0 to 0.2, η_c first slightly decreases and then increases, staying close to the prediction based on the uniform curvature assumption $\eta_c = 10.69$. However, as β increases from 0.2 to 0.8, η_c undergoes a drastic decrease. Good agreement is found between the theory and FEA regarding the stability diagram when $\alpha < 30°$ (for an intact shell, this limit can be pushed to 75° [12]). In the deep shell case ($\alpha > 30°$), the threshold η_c from FEA stays lower than the theoretical prediction, which is similar to the previous research [12]. We also capture the thresholds through experiments and qualitative agreement is found between experiments and theory (Fig. 4(d)). The experimental data points show the same trend as FEA – η_c first increases and then decreases as β increases. In addition, η_c decreases as the shell gets deeper.

To directly measure the hole's effect on the intact shell's bistability, we replace the bifurcation threshold η_c with $\lambda_c = \eta_c/\left(1-\beta^2\right) = R\alpha^2/h$ because λ_c depends only on the geometry of the intact shell. As shown in Fig. 5(a), when $\nu = 0.44$, the bifurcation threshold λ_c of a popper-like shell can be larger (regime A) or smaller than the threshold of an intact shell $\lambda_c(\beta = 0)$ depending on the relative size of the hole β. This characteristic provides us great flexibility in tuning the intact shell's bistability on demand by properly introducing a circular hole. For instance, for an intact, bistable shell with its λ ranging between the $\lambda_c(\beta = 0)$ and λ_c^m (the maximum value of λ_c), we can make it monostable by creating a hole whose size falls into the regime A (Fig. 5(a)). Likewise, a hole with its size falling into the regime B can shift an intact shell from being monostable to being bistable. Such a two-way transition adds a new, geometric variable to controlling the shell's bistability in addition to the foregoing geometric parameters of an intact shell.

In order to test whether such a non-monotonic relationship depends on the choice of the constituent material, we also plot the variation of λ_c with β when the Poisson's ratio takes on different values (Fig. 5(b)). This non-monotonic behavior is significant when $\nu > 0.2$ yet not obvious when ν approaches 0. Accordingly, we output the maximum value λ_c^m of λ_c when $\beta = 0 \sim 0.4$ and plot it versus ν in Fig. 5(c). The results show that λ_c^m increases with ν and is always higher than the bifurcation threshold of an intact shell λ_c ($\beta = 0$). Therefore, to fabricate an intact shell whose bistability is not altered due to the existence of the circular hole that may be introduced unintentionally, we

recommend that the bifurcation threshold should be chosen as λ_c^m instead of λ_c ($\beta = 0$) in practice.

In addition to the bifurcation threshold, the introduced hole also has significant impacts on the shape of the "everted" state. The maximum deflection of the "everted" shell is a quantity of particular interest in various applications. Typically, the higher the maximum deflection is, the easier it is for the bistable shell to function as an electrical switch [4] or a fluidic valve [35] where the maximum deflection dictates the shell's performance. Since the actual displacement of the inner edge under the "everted" state is equal to $w\,(r = a) = R\alpha^2\widetilde{w_0}\left(1-\beta^2\right)$, we plot the dimensionless value $\widetilde{w_0}\left(1-\beta^2\right)$ versus β to quantitatively evaluate the hole's effect on the shell's maximum deflection. As shown in Fig. 5(d), the maximum deflection undergoes a non-monotonic change when β increases. In this specific case ($\eta = 12$, $\nu = 0.44$), the maximum deflection of a popper-like shell can be larger or smaller than that of an intact shell ($\beta = 0$) when β stays in the regime B or regimes A and C, respectively (Fig. 5(d)). Therefore, the introduction of the circular hole can also be taken as an effective method to tune the maximum deflection of the bistable shell.

6. Conclusions and future directions

In this work, through a combination of experiments, theoretical modeling, and FEA, we study the bistable behavior of a popper-like shell. Four dimensionless control parameters of the shell's bistability are identified, which are η, β, α and Poisson's ratio ν. The first three depend only on the geometry of the popper-like shell while the last one is related to the mechanical property of the constituent material. Specifically, the shell undergoes a saddle–node bifurcation when η decreases to the threshold η_c with the other control parameters fixed. Accordingly, we construct the stability diagram with respect to the control parameter β and $\lambda = \eta/\left(1-\beta^2\right)$ and find that for an intact shell, its bistability is first weakened and then enhanced as the size of the defect increases, suggesting that we can transform an intact shell from being bistable to being monostable and vice versa by properly introducing this topological defect and varying its size. Such a non-monotonic variation is also observed in the maximum deflection of the shell between the "everted" shape and the natural shape, and the popper-like shell's maximum deflection can be larger or smaller than that of an intact shell with the same thickness h, radius R and subtended angle 2α, depending on the size of the defect. Therefore, the introduced circular hole can become a tunable feature in the design space of bistable shells. In addition, the established stability diagram can also be used to estimate the necessary geometry of a defected shell in a pseudo-bistable state if the viscoelasticity is considered [18], as the pseudo-bistability occurs around the bifurcation threshold of a purely elastic shell.

Apart from the geometric defect such as the circular hole discussed in this paper, there are other types of defects that may exist in the shell in practice. Those defects can be related to the geometry or material property, including, but are not limited to, multiple voids with various shapes, non-uniform thickness [36], rigid inclusion, etc. Yet their influences on the shell's mechanical behaviors and bistability remain elusive. We hope that our research will shed light on this topic and inspire new studies that address the impacts of those defects [37], the results of which will help to understand the sensitivity of the intact shell's mechanical performances to the defects that are introduced unintentionally and guide the on-demand design of these shell structures if those defects were to be created on purpose. Moreover, integrating the stimuli-responsive materials to the popper-like shell will enable the fabrication of smart components that can be applied in multiple fields including fast actuators [38,39], soft robotics [40], and other smart structures [41].

Declaration of competing interest

The authors declare that they have no known competing financial interests or personal relationships that could have appeared to influence the work reported in this paper.

Acknowledgments

The authors thank Prof. Douglas P. Holmes from Boston University for his discussion and comments. The authors acknowledge financial support from the Branco Weiss-Society in Science fellowship, administered by ETH Zürich (Z.C.), the National Institutes of Health (NIH) Director's Transformative Research Award (R01HL137157, PI: J.X.J.Z.) and the Dartmouth startup fund. Y. Liu acknowledges the support by the National Natural Science Foundation of China (11702198) and Neukom Institute Compx Faculty Grant.

Appendix A. Supplementary data

Supplementary material related to this article can be found online at https://doi.org/10.1016/j.eml.2020.101065.

References

[1] Z. Chen, Q. Guo, C. Majidi, W. Chen, D.J. Srolovitz, M.P. Haataja, Nonlinear geometric effects in mechanical bistable morphing structures, Phys. Rev. Lett. 109 (2012) http://dx.doi.org/10.1103/PhysRevLett.109.114302.
[2] G. Wan, Y. Liu, Z. Xu, C. Jin, L. Dong, X. Han, J.X.J. Zhang, Z. Chen, Tunable bistability of a clamped elastic beam, Extrem. Mech. Lett. (2019) 100603, http://dx.doi.org/10.1016/j.eml.2019.100603.
[3] A.M. Abdullah, P.V. Braun, K.J. Hsia, Programmable shape transformation of elastic spherical domes, Soft Matter. 12 (2016) 6184–6195, http://dx.doi.org/10.1039/C6SM00532B.
[4] X. Hou, Y. Liu, G. Wan, Z. Xu, C. Wen, H. Yu, J.X.J. Zhang, J. Li, Z. Chen, Magneto-sensitive bistable soft actuators: Experiments, simulations, and applications, Appl. Phys. Lett. 113 (2018) 221902, http://dx.doi.org/10.1063/1.5062490.
[5] M. Gomez, D.E. Moulton, D. Vella, Dynamics of viscoelastic snap-through, J. Mech. Phys. Solids 124 (2019) 781–813, http://dx.doi.org/10.1016/j.jmps.2018.11.020.
[6] Y. Forterre, J.M. Skotheim, J. Dumais, L. Mahadevan, How the venus flytrap snaps, Nature 433 (2005) 421–425, http://dx.doi.org/10.1038/nature03185.
[7] X. Noblin, N.O. Rojas, J. Westbrook, C. Llorens, M. Argentina, J. Dumais, The fern sporangium: A unique catapult, Science 335 (2012) 1322, http://dx.doi.org/10.1126/science.1215985.
[8] N. Hu, X. Han, S. Huang, H.M. Grover, X. Yu, L.N. Zhang, I. Trase, J.X.J. Zhang, L. Zhang, L.X. Dong, Z. Chen, Edge effect of strained bilayer nanofilms for tunable multistability and actuation, Nanoscale 9 (2017) 2958–2962, http://dx.doi.org/10.1039/C6NR08770A.
[9] B. Gorissen, D. Melancon, N. Vasios, M. Torbati, K. Bertoldi, Inflatable soft jumper inspired by shell snapping, Sci. Robot. 5 (2020) eabb1967, http://dx.doi.org/10.1126/scirobotics.abb1967.
[10] J. Yin, Z. Cao, C. Li, I. Sheinman, X. Chen, Stress-driven buckling patterns in spheroidal core/shell structures, Proc. Natl. Acad. Sci. 105 (2008) 19132–19135, http://dx.doi.org/10.1073/pnas.0810443105.
[11] S. Poppinga, M. Joyeux, Different mechanics of snap-trapping in the two closely related carnivorous plants *Dionaea muscipula* and *Aldrovanda vesiculosa*, Phys. Rev. E. 84 (2011) 041928, http://dx.doi.org/10.1103/PhysRevE.84.041928.
[12] M. Taffetani, X. Jiang, D.P. Holmes, D. Vella, Static bistability of spherical caps, Proc. R. Soc. Lond. Ser. A Math. Phys. Eng. Sci. 474 (2018) 20170910, http://dx.doi.org/10.1098/rspa.2017.0910.
[13] A. Brinkmeyer, M. Santer, A. Pirrera, P.M. Weaver, Pseudo-bistable self-actuated domes for morphing applications, Int. J. Solids Struct. 49 (2012) 1077–1087, http://dx.doi.org/10.1016/j.ijsolstr.2012.01.007.
[14] M. Santer, Self-actuated snap back of viscoelastic pulsing structures, Int. J. Solids Struct. 47 (2010) 3263–3271, http://dx.doi.org/10.1016/j.ijsolstr.2010.08.007.
[15] M. Pezzulla, N. Stoop, M.P. Steranka, A.J. Bade, D.P. Holmes, Curvature-induced instabilities of shells, Phys. Rev. Lett. 120 (2018) http://dx.doi.org/10.1103/PhysRevLett.120.048002.
[16] P.M. Sobota, K.A. Seffen, Effects of boundary conditions on bistable behaviour in axisymmetrical shallow shells, Proc. R. Soc. Lond. Ser. A Math. Phys. Eng. Sci. 473 (2017) 20170230, http://dx.doi.org/10.1098/rspa.2017.0230.

[17] K.A. Seffen, 'Morphing' bistable orthotropic elliptical shallow shells, Proc. R. Soc. Lond. Ser. A Math. Phys. Eng. Sci. 463 (2007) 67–83, http://dx.doi.org/10.1098/rspa.2006.1750.
[18] A. Madhukar, D. Perlitz, M. Grigola, D. Gai, K. Jimmy Hsia, Bistable characteristics of thick-walled axisymmetric domes, Int. J. Solids Struct. 51 (2014) 2590–2597, http://dx.doi.org/10.1016/j.ijsolstr.2014.03.022.
[19] K.A. Seffen, S. Vidoli, Eversion of bistable shells under magnetic actuation: a model of nonlinear shapes, Smart Mater. Struct. 25 (2016) 065010, http://dx.doi.org/10.1088/0964-1726/25/6/065010.
[20] D.P. Holmes, A.J. Crosby, Snapping surfaces, Adv. Mater. 19 (2007) 3589–3593, http://dx.doi.org/10.1002/adma.200700584.
[21] E. Epstein, J. Yoon, A. Madhukar, K.J. Hsia, P.V. Braun, Colloidal particles that rapidly change shape via elastic instabilities, Small 11 (2015) 6051–6057, http://dx.doi.org/10.1002/smll.201502198.
[22] J. Shim, C. Perdigou, E.R. Chen, K. Bertoldi, P.M. Reis, Buckling-induced encapsulation of structured elastic shells under pressure, Proc. Natl. Acad. Sci. 109 (2012) 5978–5983, http://dx.doi.org/10.1073/pnas.1115674109.
[23] J.L. Silverberg, A.A. Evans, L. McLeod, R.C. Hayward, T. Hull, C.D. Santangelo, I. Cohen, Using origami design principles to fold reprogrammable mechanical metamaterials, Science 345 (2014) 647–650, http://dx.doi.org/10.1126/science.1252876.
[24] A. Rafsanjani, K. Bertoldi, Buckling-induced kirigami, Phys. Rev. Lett. 118 (2017) 084301, http://dx.doi.org/10.1103/PhysRevLett.118.084301.
[25] D. Vella, Buffering by buckling as a route for elastic deformation, Nat. Rev. Phys. 1 (2019) 425–436, http://dx.doi.org/10.1038/s42254-019-0063-1.
[26] N. Hu, D. Chen, D. Wang, S. Huang, I. Trase, H.M. Grover, X. Yu, J.X.J. Zhang, Z. Chen, Stretchable Kirigami polyvinylidene difluoride thin films for energy harvesting: Design, analysis, and performance, Phys. Rev. Appl. 9 (2018) 021002, http://dx.doi.org/10.1103/PhysRevApplied.9.021002.
[27] P.M. Sobota, K.A. Seffen, Multistable slit caps, in: Proceedings of the IASS Annual Symposium 2016, International Association for Shell and Spatial Structures (IASS), Tokyo, Japan, 2016, pp. 1–10.
[28] E. Ventsel, T. Krauthammer, Thin Plates and Shells: Theory, Analysis, and Applications, Marcel Dekker, New York, 2001.
[29] K.A. Seffen, C. Maurini, Growth and shape control of disks by bending and extension, J. Mech. Phys. Solids 61 (2013) 190–204, http://dx.doi.org/10.1016/j.jmps.2012.08.003.
[30] Y. Liu, S. Liang, Q. Huang, H. Hu, Y. Zheng, H. Zhang, Q. Shao, A robust riks-like path following method for strain-actuated snap-through phenomena in soft solids, Comput. Methods Appl. Mech. Engrg. 323 (2017) 416–438, http://dx.doi.org/10.1016/j.cma.2017.05.010.
[31] E. Riks, An incremental approach to the solution of snapping and buckling problems, Int. J. Solids Struct. 15 (1979) 529–551, http://dx.doi.org/10.1016/0020-7683(79)90081-7.
[32] J. Lin, Q. Guo, S. Dou, N. Hua, C. Zheng, Y. Pan, Y. Huang, Z. Chen, W. Chen, Bistable structures with controllable wrinkled surface, Extrem. Mech. Lett. 36 (2020) 100653, http://dx.doi.org/10.1016/j.eml.2020.100653.
[33] W. Hamouche, C. Maurini, A. Vincenti, S. Vidoli, Basic criteria to design and produce multistable shells, Meccanica 51 (2016) 2305–2320, http://dx.doi.org/10.1007/s11012-016-0375-5.
[34] C.G. Diaconu, P.M. Weaver, A.F. Arrieta, Dynamic analysis of bi-stable composite plates, J. Sound Vib. 322 (2009) 987–1004, http://dx.doi.org/10.1016/j.jsv.2008.11.032.
[35] M. Gomez, D.E. Moulton, D. Vella, Passive control of viscous flow via elastic snap-through, Phys. Rev. Lett. 119 (2017) http://dx.doi.org/10.1103/PhysRevLett.119.144502.
[36] A. Lee, D. Yan, M. Pezzulla, D.P. Holmes, P.M. Reis, Evolution of critical buckling conditions in imperfect bilayer shells through residual swelling, Soft Matter. 15 (2019) 6134–6144, http://dx.doi.org/10.1039/C9SM00901A.
[37] D. Yan, M. Pezzulla, P.M. Reis, Buckling of pressurized spherical shells containing a through-thickness defect, J. Mech. Phys. Solids 138 (2020) 103923, http://dx.doi.org/10.1016/j.jmps.2020.103923.
[38] Q. Zhao, X. Yang, C. Ma, D. Chen, H. Bai, T. Li, W. Yang, T. Xie, A bioinspired reversible snapping hydrogel assembly, Mater. Horiz. 3 (2016) 422–428, http://dx.doi.org/10.1039/C6MH00167J.
[39] X. Yang, G. Li, T. Cheng, Q. Zhao, C. Ma, T. Xie, T. Li, W. Yang, Bio-inspired fast actuation by mechanical instability of thermoresponding hydrogel structures, J. Appl. Mech. 83 (2016) 071005, http://dx.doi.org/10.1115/1.4032983.
[40] P. Rothemund, A. Ainla, L. Belding, D.J. Preston, S. Kurihara, Z. Suo, G.M. Whitesides, A. soft, Bistable valve for autonomous control of soft actuators, Sci. Robot. 3 (2018) eaar7986, http://dx.doi.org/10.1126/scirobotics.aar7986.
[41] Q. Guo, Y. Pan, J. Lin, G. Wan, B. Xu, N. Hua, C. Zheng, Y. Huang, Y. Mei, W. Chen, Z. Chen, Programmable 3D self-folding structures with strain engineering, Adv. Intell. Sys. (2020) 2000101, http://dx.doi.org/10.1002/aisy.202000101.